Wind Shear and Buoyancy Reversal at the Top of Stratocumulus

JUAN PEDRO MELLADO AND BJORN STEVENS

Max Planck Institute for Meteorology, Hamburg, Germany

HEIKO SCHMIDT

Brandenburg University of Technology, Cottbus, Germany

(Manuscript received 27 June 2013, in final form 30 October 2013)

ABSTRACT

A numerical experiment is designed to study the interaction at the stratocumulus top between a mean vertical shear and the buoyancy reversal due to evaporative cooling, without radiative cooling. Direct numerical simulation is used to eliminate the uncertainty introduced by turbulence models. It is found that the enhancement by shear-induced mixing of the turbulence caused by buoyancy reversal can render buoyancy reversal comparable to other forcing mechanisms. However, it is also found that (i) the velocity jump across the capping inversion Δu needs to be relatively large and values of about $1\,\mathrm{m\,s^{-1}}$ that are typically associated with the convective motions inside the boundary layer are generally too small and (ii) there is no indication of cloud-top entrainment instability. To obtain these results, parameterizations of the mean entrainment velocity and the relevant time scales are derived from the study of the cloud-top vertical structure. Two overlapping layers can be identified: a background shear layer with a thickness $(1/3)(\Delta u)^2/\Delta b$, where Δb is the buoyancy increment across the capping inversion and a turbulence layer dominated by free convection inside the cloud and by shear production inside the relatively thin overlap region. As turbulence intensifies, the turbulence layer encroaches into the background shear layer and defines thereby the entrainment velocity. Particularized to the first research flight of the Second Dynamics and Chemistry of the Marine Stratocumulus (DYCOMS II) field campaign, the analysis predicts an entrainment velocity of about $3\,\mathrm{mm\,s^{-1}}$ after 5–10 min—a velocity comparable to the measurements and thus indicative of the relevance of mean shear in that case.

1. Introduction

The deepening of the stratocumulus-topped boundary layer (STBL) as nonturbulent fluid is imbued with the properties of the turbulent layer, or entrained, plays a key role in the temporal evolution of the boundary layer as a whole. The relatively thin region where this entrainment occurs, which we shall call the entrainment interfacial layer (EIL), comprises the upper part of the cloud layer, the cloud boundary itself, the turbulent–nonturbulent interface, and the relatively smooth transition to the troposphere above it. The interaction among the different local processes in this region and the resulting entrainment rates still remain largely unclear (see, e.g., Stevens 2002; Wood 2012).

A longstanding question has been to what extent buoyancy reversal occurring as a result of diabatic mixing between saturated and unsaturated air within the EIL might not only destabilize the layer locally, leading to the onset of downward directed convection, but also globally, as more convection is associated with more mixing, which causes more convection and the eventual desiccation of the STBL as a whole (Deardorff 1980; Randall 1980). Mellado et al. (2009) and Mellado (2010) demonstrated that the presence of buoyancy reversal alone leads to a metastable layer as the mixing rate, or entrainment rate, is diffusively limited, so that the eventual breakup of the cloud by buoyancy reversal alone occurs on time scales that are much too long to be relevant to the STBL. However, these earlier results left open the possibility that buoyancy reversal, when augmented by other sources of turbulence, might cease to be diffusively limited and thus play a greater role than one would be led to believe by the consideration of buoyancy reversal alone.

Corresponding author address: Juan Pedro Mellado, Max Planck Institute for Meteorology, Bundesstr. 53, 20146 Hamburg, Germany.
E-mail: juan-pedro.mellado@mpimet.mpg.de

DOI: 10.1175/JAS-D-13-0189.1

In addition to buoyancy reversal, both the vertical shear of the horizontal wind across the EIL and further convective driving through radiative cooling of the cloud-top region act as local sources of turbulence. In this paper, we extend the work of Mellado et al. (2009) and Mellado (2010) by exploring the role of shear and its possible interaction with buoyancy reversal.

Expanding on earlier work through a study of the role of shear is interesting for at least two reasons. First, shear is ubiquitous, as local shear associated with large-scale eddies will also be evident even in the absence of a mean wind. Second, shear alone cannot sustain a continuous deepening of the layer, as shear generated turbulence will locally thicken the EIL, but in the absence of other sources, the turbulence will eventually decay once a critical EIL thickness is reached. The latter makes it interesting to combine shear with the convective destabilization of the cloud-top layer through buoyancy reversal, as neither process acting alone is efficient in supporting significant mixing at the cloud top. In contrast, by generating convective eddies that locally thin the EIL, buoyancy reversal might help enhance shear, which in turn locally enhances the mixing that sustains the buoyancy reversal, raising the possibility that the processes are self-reinforcing.

Despite a steady trickle of observational studies (e.g., Caughey et al. 1982; Faloona et al. 2005; de Roode and Wang 2007; Katzwinkel et al. 2012; Malinowski et al. 2013) and some numerical investigations (e.g., Wang et al. 2008; Kurowski et al. 2009), suggesting an important role for shear within the EIL, theoretical and modeling studies typically focus on shear-free cases and neglect the effects of local shear within the EIL. The reason for this may be that mean shear and convective effects are hard to realize together in laboratory experiments. Large-eddy simulation (LES) is also not well suited to a consideration of the small-scale processes occurring within the EIL—a layer that is often too thin to be well resolved by an LES focused on the evolution of the boundary layer as a whole. And measurements of the EIL in natural flows are difficult and expensive to make. Consequently, understanding of how shear and convection interact within the EIL, and the importance of such interaction for the dynamics of the STBL, remain limited. However, to the extent that direct numerical simulation (DNS) is able to reach flow regimes evincing some degree of Reynolds number similarity (Tennekes and Lumley 1972; Dimotakis 2000; Monin and Yaglom 2007), it might be possible to fill the gap in the available empiricism and advance understanding (Moin and Mahesh 1998). Advances in computing power have begun to make such DNS-based approaches conceivable, and have motivated a number of recent studies (Abma et al. 2013; de Lozar and Mellado 2013), including the present one.

Specifically, in the present analysis we build on the earlier study by Mellado et al. (2009) and Mellado (2010) to ask the following: Can shear render buoyancy reversal as important as radiative cooling in driving convective motion? Can it lead to a desiccation of the cloud? To answer these questions, we first derive a parameterization of the mean entrainment velocity and relevant time scales using DNS of an appropriately defined problem, and we then rescale the results to typical atmospheric conditions based on the observed Reynolds number similarity. We do it as follows. Section 2 describes the experimental setup, the so-called cloud-top mixing layer, and the bulk formulation employed in the analysis. Section 3 summarizes previous results on the instabilities driving the system, which already provides some of the length, time, and velocity scales characterizing the cloud-top dynamics. Section 4 provides the necessary characterization of the EIL vertical structure, including the definition of the mean entrainment velocity w_e used in the analysis. Section 5 obtains the relevant velocity scales of the turbulence inside of the cloud and inside of the EIL. The parameterization of w_e in terms of the velocity and buoyancy increments across the EIL and the buoyancy reversal parameters is presented and discussed in section 6. Implications of the results for the STBL are analyzed in section 7, before the summary and concluding remarks.

2. Formulation

The definition of the cloud-top mixing layer and the two-fluid formulation used to study latent heat effects is based on the early work by Bretherton (1987) and it has been thoroughly described in Mellado et al. (2010). The cloud-top mixing layer consists of a region of dry, warm air, representing the free atmosphere, on top of a region of moist, relatively cold air, representing the cloud layer. Each of the two layers is assumed to have a well-defined homogeneous thermodynamic state and horizontal velocity, as sketched in Fig. 1. The mixture fraction χ is equal to the total enthalpy and total water contents conveniently normalized with the state in each of the layers. In the two-fluid formulation employed here, these two thermodynamic variables obey an advection–diffusion equation and therefore χ is equal to the fraction of mass proceeding from one of the two layers. Without loss of generality, we choose the value $\chi = 0$ to represent the in-cloud fluid and $\chi = 1$ to represent the free-atmosphere fluid. The frame of reference is chosen to move with the mean velocity between the two layers and the streamwise direction Ox is aligned with the velocity difference vector, whose magnitude is Δu.

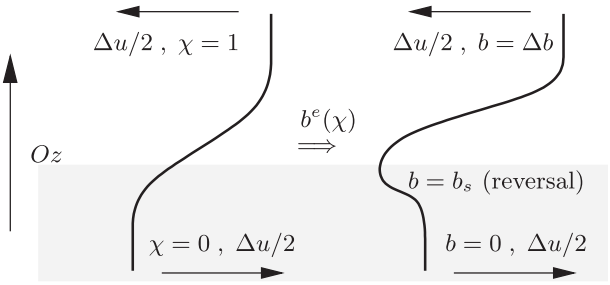

FIG. 1. Defining sketch of the cloud-top mixing layer. The mixture fraction χ (normalized enthalpy and total water content) varies between 0 inside the cloud layer (gray color) and 1 inside the free atmosphere above. The corresponding variation of the buoyancy is Δb. The velocity difference across the cloud top is Δu.

The governing equations are

$$\left.\begin{aligned} \partial \mathbf{v}/\partial t + \nabla \cdot (\mathbf{v} \otimes \mathbf{v}) &= -\nabla p + \nu \nabla^2 \mathbf{v} + b\mathbf{k} \\ \nabla \cdot \mathbf{v} &= 0 \\ \partial \chi/\partial t + \nabla \cdot (\mathbf{v}\chi) &= \kappa \nabla^2 \chi \\ b &= b^e(\chi) \end{aligned}\right\}. \quad (1)$$

The velocity vector is $\mathbf{v} = (u, v, w)$, w being the vertical component, the kinematic viscosity is ν, κ is the scalar diffusivity, p is a kinematic pressure, and $\mathbf{k}$ is the unit vector along the vertical direction Oz. The system is statistically homogeneous inside the horizontal planes, and the data inside these planes are used to construct the different statistics, which depend then on the vertical coordinate z and the time t. Averaged values are indicated by angle brackets and the corresponding fluctuations by the prime.

Thermodynamic equilibrium is assumed. The resulting buoyancy function $b^e(\chi)$, a one-to-one mapping between mixing fraction and buoyancy, is valid as long as the domain under study is small enough to neglect vertical variation of the thermodynamic pressure. From calculations of the exact thermodynamic equilibrium, it is observed (Fig. 2) that $b^e(\chi)$ is very well approximated by

$$\frac{b^e(\chi)}{\Delta b} = -\frac{D}{\chi_s}\chi + Q\delta_s \ln\left[\exp\left(\frac{\chi - \chi_s}{\delta_s}\right) + 1\right], \quad (2)$$

a smoothed, piecewise linear function where $Q = (\chi_s + D)/[\chi_s(1 - \chi_s)]$ is a nondimensional vaporization enthalpy, δ_s is a smoothing factor that regularizes the phase changes, χ_s is the saturation mixture fraction, and

$$D = -\frac{b_s}{\Delta b} \quad (3)$$

is the buoyancy reversal parameter, where b_s is the saturation buoyancy as obtained from the equilibrium

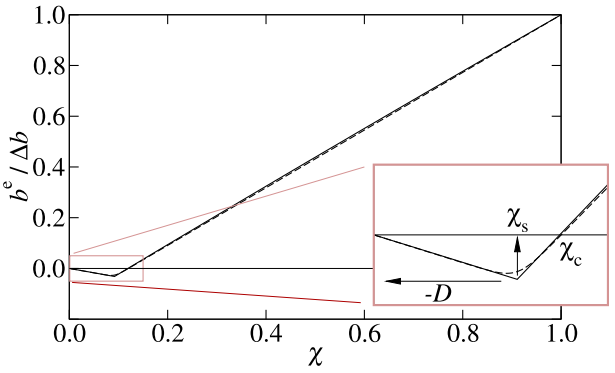

FIG. 2. Buoyancy function $b^e(\chi)$ for thermodynamic conditions measured during the first research flight of the DYCOMS II field campaign (cases H11 and M11 in Table 1). Solid line represents exact equilibrium and the dashed line [which lies almost on top of the solid line except near the $(\chi_s, -D)$ point as better seen in the inset] is an approximation according to Eq. (2).

calculation and Δb is the buoyancy increment across the cloud top. If $b_s < 0$, then buoyancy reversal is said to occur (Siems et al. 1990; Wunsch 2003). The cloud (condensate) corresponds to mixtures $\chi < \chi_s$. The crossover mixture fraction

$$\chi_c = \frac{\chi_s + D}{1 + D} \quad (4)$$

defines the upper limit to mixtures that are negatively buoyant. The parameter δ in Eq. (2) smooths ∇b at the saturation surface $\chi(\mathbf{x}, t) = \chi_s$, which, under the assumption of strict equilibrium (i.e., phase change being instantaneous), would otherwise be a delta function (Mellado et al. 2010).

Because we are interested in the fully developed turbulent regime, which is established after the details of the initial conditions have been sufficiently forgotten, the flow we consider can be completely specified by the parameters (Δu, Δb, κ, ν, b_s, χ_s). These parameters identify four nondimensional numbers (Pr, D, χ_s, Re_0) when Δu and Δb are used to normalize the other parameters. In this work, the Prandtl number $\mathrm{Pr} = \nu/\kappa$ is set to 1. The reference Reynolds number is

$$\mathrm{Re}_0 = (1/3)\frac{(\Delta u)^3}{\nu \Delta b}. \quad (5)$$

The prefactor 1/3 is introduced based on existing knowledge from cloud-free, stably stratified shear layers and is discussed further in the following section.

The set of configurations analyzed is summarized in Table 1 and it is exactly the same as that investigated in the shear-free case by Mellado (2010). The thermodynamic state of the reference cases H11 and M11 (which

TABLE 1. Simulation series. Thermodynamic state for reference cases M11 and H11 taken from RF01/DYCOMS II (Stevens et al. 2003a): ΔT_l is the jump across the cloud-top region in liquid-water static energy temperature (°C), Δq_t is the jump in total water content, and $q_{l,c}$ is the cloud liquid-water content ($g\,kg^{-1}$). Cases M21 and M12 derived to investigate the effects of the buoyancy reversal parameters D and χ_s independently, maintaining the same buoyancy increment $\Delta b = 0.25\,m\,s^{-2}$. Simulation L00 corresponds to a stably stratified shear layer without buoyancy reversal (Brucker and Sarkar 2007). The velocity increment Δu ($m\,s^{-1}$) is calculated according to Eq. (5) and the thickness h_S (m) is calculated according to Eq. (6). The turbulent Reynolds number $Re_t = e^2/(\varepsilon\nu)$, where e is the turbulence kinetic energy and ε its viscous dissipation rate, is the maximum in-cloud value.

	D	χ_s	χ_c	Re_0	ΔT_l	Δq_t	$q_{l,c}$	Δu	h_S	Grid	Re_t	c_1	c_2	c_3
H11	0.031	0.09	0.117	2.2×10^4	9.7	−7.5	0.5	0.63	0.53	$3072^2 \times 2216$	3800	0.022	−0.11	5.9
M11	0.031	0.09	0.117	1.1×10^4	9.7	−7.5	0.5	0.50	0.33	$2048^2 \times 1664$	1800	0.021	−0.11	6.2
M21	0.062	0.09	0.143	1.1×10^4	8.5	−8.4	0.5	0.50	0.33	$2048^2 \times 1664$	3200	0.034	−0.09	4.7
M12	0.031	0.18	0.205	1.1×10^4	13	−8.2	1.2	0.50	0.33	$2048^2 \times 1664$	2300	0.018	−0.06	7.4
L00	0.0	0.0	0.0	3.7×10^3	9.7	−7.5	0.0	0.35	0.16	$1024^2 \times 832$	—	—	—	—

only differ in the Reynolds number, as indicated by the leading character) corresponds to field measurements of nocturnal marine stratocumulus obtained during the first research flight (RF01) of the Second Dynamics and Chemistry of the Marine Stratocumulus (DYCOMS II) field campaign (Stevens et al. 2003a). Case M21 differs from the reference case M11 through a doubling of D, and case M12 differs through a doubling of χ_s.

The reference Reynolds number we can reach with a grid $2048 \times 2048 \times 1664$ is $Re_0 = 1.1 \times 10^4$, having a resolution parameter $\Delta x/\eta \simeq 1.25$ at the end of the simulation, where Δx is the grid spacing and η the Kolmogorov scale. Using $\nu = 1.5 \times 10^{-5}\,m^2\,s^{-1}$ for the kinematic viscosity of air in typical atmospheric conditions, this Reynolds number corresponds to $\Delta u = 0.5\,m\,s^{-1}$ and a domain size of 6.6 m for the reference RF01/DYCOMS II case, where $\Delta b = 0.25\,m\,s^{-2}$. The reference case M11 is repeated in simulation H11 at a double Reynolds number $Re_0 = 2.2 \times 10^4$ to ascertain possible Reynolds number effects. For this case H11, the domain size is about 12 m. By comparing one to one the results from cases M11 and H11, it will be demonstrated that Reynolds number similarity already applies to some of the relevant statistics and thus justifies the extrapolation of the results to atmospheric values (Tennekes and Lumley 1972; Monin and Yaglom 2007).

Finite differences are used to solve the previous set of equations using Cartesian coordinates and a structured grid. Sixth-order spectral-like compact schemes are employed to resolve with fidelity the molecular processes (Lele 1992). The discrete solenoidal constraint is imposed using Fourier decomposition along the periodic horizontal planes x_1Ox_2 and a factorization of the resulting set of equations along the vertical coordinate (Mellado and Ansorge 2012). A low-storage fourth-order accurate Runge–Kutta scheme is used to advance in time (Carpenter and Kennedy 1994). At the top and bottom boundaries of the computational domain, no-penetration free-slip boundary conditions are used. Preliminary work was used to place these boundaries far enough to assure a negligible influence in the results, to ascertain the resolution requirements, and to assess the influence of δ_s whose value is set to 0.09/16. Further details of choices made in the setup of the experiments are discussed in Mellado (2010).

3. Preliminaries

Wind shear alone cannot sustain turbulence inside the capping inversion except for a relatively short period of time. However, it can enhance the turbulence caused by buoyancy reversal. The understanding and quantification of this interaction between shear and buoyancy reversal is the aim of this paper and this section introduces the main elements of this interaction: The concept of the background shear layer provides the reference structure, including the length scale h_S, and it is presented first. Then, the mechanisms destabilizing that shear layer are briefly reviewed, introducing one of the velocity scales characterizing the system w_R and anticipating the dependence of the resulting mean entrainment velocity w_e on some details of these destabilizing mechanisms.

a. Formation of the background shear layer

In the absence of buoyancy reversal the problem we consider reduces to that of shear driven mixing layers in the presence of stratification (see, e.g., Sherman et al. 1978; Thorpe 1987; Peltier and Caulfield 2003; Mashayek and Peltier 2011). If the initial shear layer is sufficiently thin, Kelvin–Helmholtz instabilities will cause an overturning of the layer and a thickening of the interface around its center at $z = z_0$ until it reaches an asymptotic thickness

$$h_S = (1/3)\frac{(\Delta u)^2}{\Delta b}. \tag{6}$$

(The subscript S indicates "shear.") The value of 1/3 is well established (±15%) by laboratory and numerical studies (see, e.g., Smyth and Moum 2000; Brucker and

Sarkar 2007) and can be associated with a critical value of the bulk Richardson number $\mathrm{Ri}_b = h_\omega \Delta b/(\Delta u)^2$, which is defined in terms of the basic parameters of the problem and the vorticity thickness

$$h_\omega = \frac{\Delta u}{(\partial \langle u \rangle / \partial z)_{\max}}. \tag{7}$$

[A similar behavior based on a critical bulk Richardson number has also been observed in the entrainment zone of cloud-free, sheared convective boundary layers (Conzemius and Fedorovich 2007).] The reference Reynolds number, Eq. (5), can then be written as $\mathrm{Re}_0 = h_S \Delta u/\nu$. The asymptotic thickness of the shear layer also introduces a time scale

$$t_S = \frac{h_S}{\Delta u} = (1/3)\frac{\Delta u}{\Delta b}, \tag{8}$$

which is comparable to the time scale $\sqrt{h_S/\Delta b}$ associated with a restoring force that is proportional to Δb. This process is represented by case L00 in Fig. 3: After a linear growth during a time $\simeq 10 t_S$, the quantity $h_\omega(t)$ bends toward h_S; this transition requires $\simeq 20 t_S$. We will refer to this asymptotic state as the background shear layer.

The formation of a background shear layer as described in the previous paragraph is often faster than other mixing processes affecting the cloud-top dynamics, like large-scale convective motions induced by radiative or evaporative cooling, and therefore h_S is expected to characterize, at least in part, the cloud-top region. For instance, for typical atmospheric conditions $\Delta u \simeq 1-10\,\mathrm{m\,s^{-1}}$ and $\Delta b \simeq 0.1-0.3\,\mathrm{m\,s^{-2}}$ (temperature difference across the capping inversion of approximately 3–9 K), the time scales of the order of $10 t_S$ involved in the formation of the background shear layer vary between a few tens of seconds and a few minutes (longer times for a stronger velocity difference or a weaker stratification), whereas the time scales associated with the large-scale convective motions are $\simeq 20$ min. Figure 3 supports the previous argument: After $\simeq 5 - 10 t_S$, buoyancy reversal starts to modify the background shear layer but the vorticity thickness h_ω in cases M11 and H11, though reduced with respect to the case L00 without buoyancy reversal, remains comparable to h_S during the rest of the simulation. (See also Fig. 4.) Section 4 will further confirm this relevance of h_S.

To conclude, we note that differences in the normalized velocity and buoyancy profiles imposed by the initial conditions or, in our case, implied by the nonlinear relation between b and χ, Eq. (2) and Fig. 2, can lead to a shear-layer formation that is more complex than what has been here summarized (Smyth et al. 2007; Carpenter et al. 2007). However, these effects are expected to be small because atmospheric values of D and χ_s are typically small, and, moreover, we are mainly interested in the turbulence regime that is established after the formation of the background shear layer.

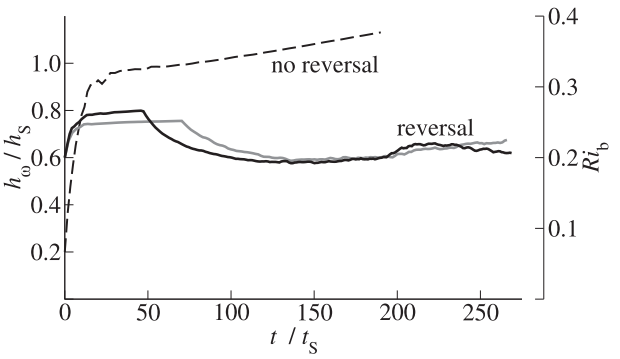

FIG. 3. Temporal evolution of the normalized vorticity thickness h_ω/h_S [or, equivalently, bulk Richardson number $\mathrm{Ri}_b = h_\omega \Delta b/(\Delta u)^2 = (1/3)h_\omega/h_S$]: solid black line is case H11, dashed line is case L00 without buoyancy reversal, and solid gray line is case M11 with half the Reynolds number of H11.

b. Destabilization of the background shear layer

On time scales that are long compared to the development of the background shear layer, buoyancy reversal destabilizes the system in two ways. First, the lower part of the background shear layer, approximately $\chi_c h_S$, becomes negatively buoyant and tends to fall away from, or peel off, that layer (Fig. 4c). Previous analysis on the shear-free, buoyancy-reversal instability (Mellado et al. 2009) suggests using

$$t_R = \sqrt{h_S/|b_s|} = 1/\sqrt{3D}\ \frac{\Delta u}{\Delta b}, \tag{9}$$

and

$$w_R = \sqrt{h_S |b_s|} = \sqrt{D/3}\,\Delta u \tag{10}$$

as reference time and velocity scales for the effects of buoyancy reversal (the subscript R stands for "reversal"). The results discussed during the following sections confirm that these scales help to characterize the turbulence state also in the configuration with an imposed wind shear as considered in this paper. Mechanistically, w_R can be identified with the terminal velocity resulting from the balance between the buoyancy force acting on a parcel of fluid of volume $\propto h_S^3$ and the aerodynamic drag experienced by that parcel of fluid, which is proportional to a cross-section h_S^2; that is, $\rho_0 |b_s| h_S^3 \simeq \rho_0 w_R^2 h_S^2$. These buoyancy-reversal scales can also be understood in terms of the free-fall motion over a length h_S associated with a reduced gravity $|b_s|$.

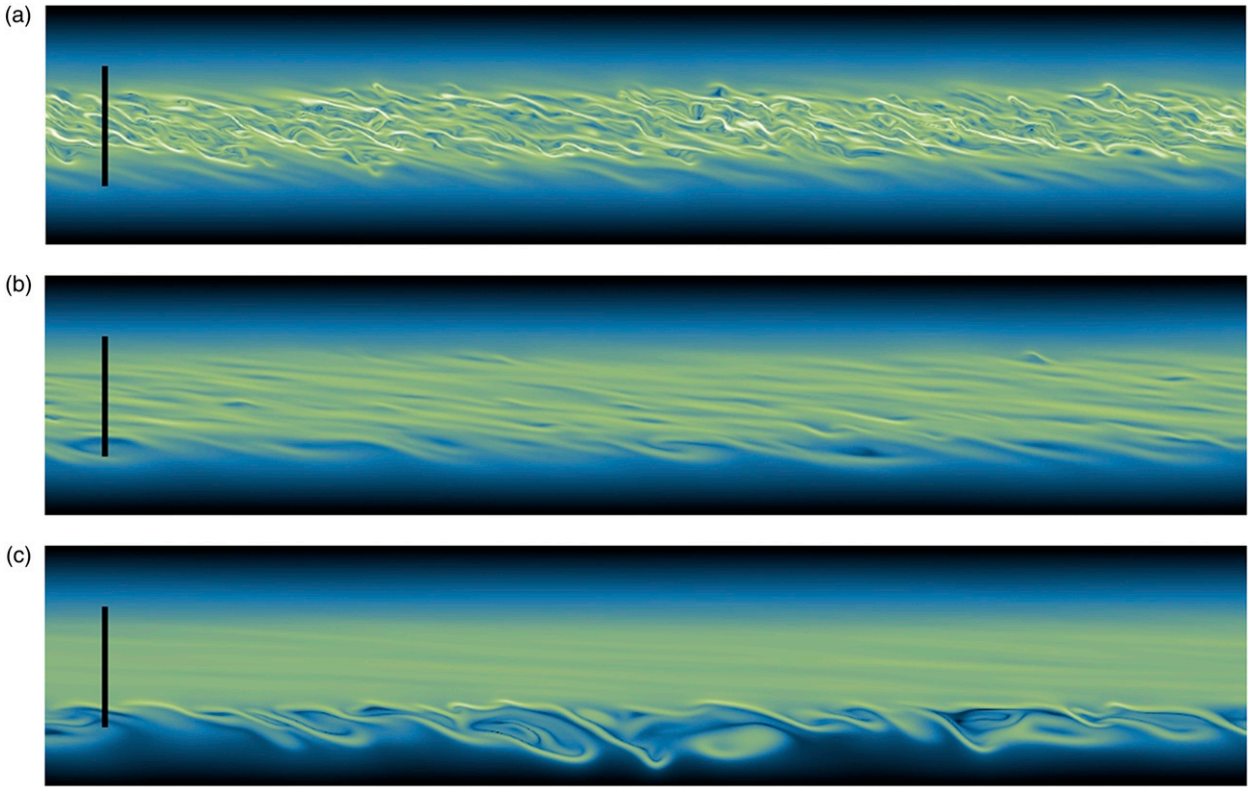

FIG. 4. (top to bottom) Sequence of cross sections showing, in terms of the scalar dissipation rate $\kappa|\nabla\chi|^2$, the relatively fast decay of the turbulence inside the background shear layer compared to the relatively slow development of the buoyancy reversal instability at the base: $t = t_S \times$ (a) 1.5, (b) 2.9, and (c) 4.3. Illustrated in (c) are the mixtures at the bottom falling down and being rolled into billows, strongly flattened because of the stable stratification. (This provides detail at early times of the information portrayed in Fig. 5d.)

Evaporative cooling without buoyancy reversal, $-\chi_s < D < 0$, yields a stably stratified system that supports gravity waves. The complex number obtained in Eq. (10) when $D < 0$ indicates the associated oscillatory motion as obtained by the linear stability analysis [see Mellado et al. (2009) for more details]. However, this condition does not destabilize the background shear layer into a turbulent state. Therefore, only buoyancy reversal conditions are of interest and we consider $D > 0$ hereafter.

The second destabilizing mechanism is the excitation of the shear layer from below due to the in-cloud turbulent fluctuations. This problem is still a matter of research within the context of turbulent mixing across a density interface (see, e.g., Fernando 1991; Strang and Fernando 2001). The cloud top is, in principle, even more challenging because the forcing occurs at the interface itself instead of being imposed away from it. However, there is one simplifying feature: Eq. (10) implies that the intensity of the velocity fluctuations generated by buoyancy reversal, comparable to w_R, is small compared to the velocity difference across the inversion, Δu, since $w_R/\Delta u = \sqrt{D/3}$ and $\sqrt{D/3} \ll 1$ under typical atmospheric conditions. This property can be used to anticipate that, since buoyancy reversal is the ultimate destabilizing mechanism and therefore source of turbulence, there is an interval of time in which the in-cloud velocity fluctuations remain small compared to Δu and therefore the vertical distortion of the background shear layer is relatively small, independently of the size of the in-cloud integral length scale.

As the in-cloud turbulence intensifies, turbulence penetrates deeper into the background shear layer, defining thereby a mean entrainment velocity w_e. The analysis of the evolution equation for the turbulence kinetic energy will show that turbulence entrainment is concentrated in a thin region that behaves similarly to stably stratified sheared turbulence and that we can estimate w_e from

$$w_e \Delta b \sim P_0, \tag{11}$$

where P_0 is a characteristic scale of the turbulence production rate by mean shear. The aim of the following sections is to understand this relation, in particular, the dominant balance in the evolution equation for the turbulence kinetic energy where it comes from, and to estimate P_0 and thereby w_e.

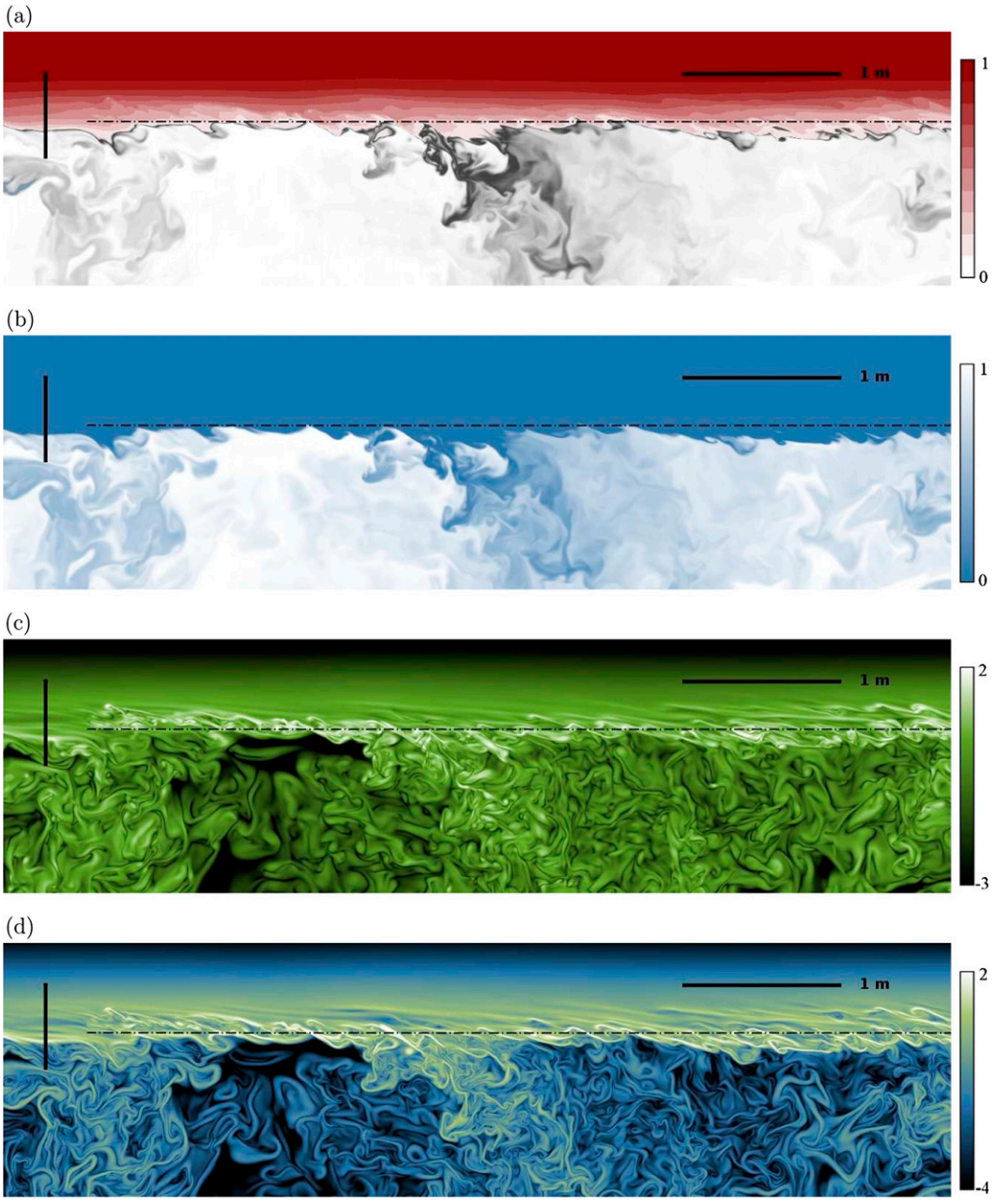

FIG. 5. Vertical cross sections for case H11 at the final time $t_2/t_R = 27.1$ ($\simeq$4 min). (a) Mixture fraction χ (normalized enthalpy and total water content) in binned, reddish colors (scale is 0 to 1); gray indicates negatively buoyant regions, the buoyancy varying between $b_s < 0$ (black) and 0 (white). (b) Liquid mass fraction normalized with the in-cloud value $q_l/q_{l,c}$ (scale is 0 to 1). (c) Normalized enstrophy $\log_{10}(t_S^2|\nabla u|^2)$ (scale is -3 to 2). (d) Normalized scalar dissipation rate (scale is -4 to 2). The vertical bars at the top-left corner of each panel indicate the extent h_S of the background shear layer, centered at $z = z_0$ [Eq. (6)]. The horizontal dotted–dashed lines in each panel correspond to the reference height z_i [Eq. (13)], and the black horizontal line at the top-right corner of each panel is included to give a 1-m-length-scale reference. This figure shows only 1/2 × 1/5 of the domain.

4. Entrainment interfacial layer

For the strong-shear regime $\Delta u/w_R \gg 1$ considered in this paper and explained in the previous section, the entrainment interfacial layer or EIL consists of a relatively thin and flat region of thickness $\simeq h_S$ encompassing the remnant of the background shear layer, centered at $z = z_0$, and the roots of the convective motions that

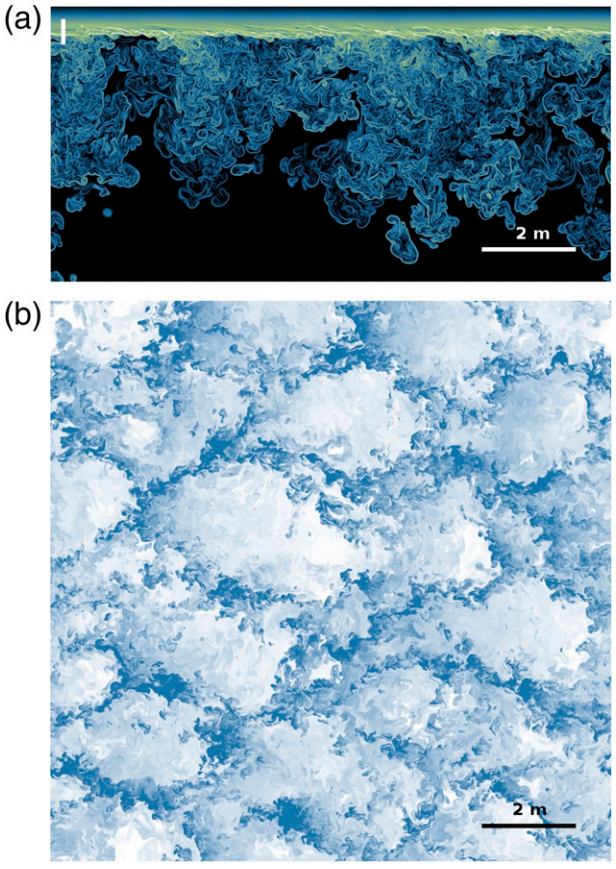

FIG. 6. Cross sections over the complete domain for case H11 at the final time $t_2/t_R = 27.1$ ($\simeq$4 min): (a) scalar dissipation rate as in Fig. 5d, where the vertical bar at the top-left corner indicates the extent h_S of the background shear layer, centered at $z = z_0$ [Eq. (6)] and (b) horizontal cross section at the inversion base $z = -h_S/2$ of the normalized liquid content $q_l/q_{l,c}$ (color map is as in Fig. 5b). The horizontal bars at each panel's bottom-right corner provide a 1-m-length-scale reference.

plummet downward into the cloud (Figs. 5 and 6). This section emphasizes features of this vertical structure that are useful for the understanding of the entrainment process and the derivation of the corresponding mean entrainment velocity.

The mean shear concentrates at the EIL and it does not extend significantly into the cloud layer (Fig. 7a), the maximum value being $(\partial\langle u\rangle/\partial z)_{\max} = \Delta u/h_\omega \simeq (3/2)\Delta u/h_S$ (since $h_\omega/h_S \simeq 2/3$, from Fig. 3). The same behavior is observed in the mean gradient of the mixture fraction (normalized enthalpy and total water content) and of the buoyancy (Fig. 7b).

We can distinguish two regions within the EIL. The lower half is characterized by strong turbulent mixing, as indicated by the large values of enstrophy $|\nabla \times \mathbf{u}|^2$ (Fig. 5c) and scalar dissipation rate $\kappa|\nabla\chi|^2$ (Fig. 5d). The buoyancy field attains its most negative values in this lower half of the EIL, since the mean position of the cloud boundary lies there (Fig. 7c) and evaporative cooling concentrates near the cloud boundary (Figs. 5a,b). In contrast, the upper part the EIL is relatively well mixed and provides a smooth transition of the moisture and temperature fields between the cloud and the free troposphere. [This asymmetric vertical structure and the coexistence of Kelvin–Helmholtz billows with Holmboe wavelike disturbances is not only intrinsic to the EIL here considered, but also commonly found in other cloud-free, shear configurations with similar stratification conditions (Strang and Fernando 2001).]

The distinction of two regions within the EIL is further exposed by the profile of the gradient Richardson number (Fig. 7d): The behavior in the upper half corresponds to that found in stably stratified shear layers (see, e.g., Smyth and Moum 2000), as expected. However, it increases sharply up to 0.5 in the lower half of the EIL before becoming negative inside the convectively unstable region. This supercritical value is not inconsistent with the presence of turbulence there, since this turbulence is forced externally from below and not only by the local mean shear. Moreover, the nonlinear relation between b and χ—see Eq. (2) and Fig. 2—also favors these supercritical conditions.

The penetration, or encroachment, of the turbulent region into the upper, nonturbulent part of the EIL is inferred by comparing the profiles at the two different times that are included in Fig. 7 (dashed and solid lines), especially the bottom row Figs. 7e–h. Figure 7h is particularly useful for this purpose because the rapid fall to zero of the viscous dissipation rate $\varepsilon = \langle \nu(u'_{i,j} + u'_{j,i})u'_{i,j}\rangle$ around the center of the EIL quantifies the mean position of the turbulent–nonturbulent interface, since the average magnitude of the vorticity fluctuation (not shown) is very similar to that of ε and the turbulent region is defined by a nonzero vorticity fluctuation (Pope 2000). Note that, in contrast, the mean vorticity profile $\partial\langle u\rangle/\partial z$ extends deeper upward, as deduced from the molecular flux profile in Fig. 7e; this distinction between the mean and the fluctuating vorticity fields is also illustrated in Fig. 5c. The broader profile of scalar fluctuation compared to that of ε (Fig. 7g) suggests gravity wave activity in the upper part of the EIL.

The entrainment process can be further analyzed with the aid of the evolution equation for the turbulence kinetic energy

$$\frac{\partial e}{\partial t} = -\frac{\partial T}{\partial z} + P + B - \varepsilon, \tag{12}$$

where $T = \langle w'u'_iu'_i/2 + p'w' - u'_i\tau'_{iz}\rangle$ is the turbulent flux along the vertical direction, $P = -\langle u'w'\rangle\partial\langle u\rangle/\partial z$ is the turbulence production rate by mean shear, $B = \langle w'b'\rangle$ is

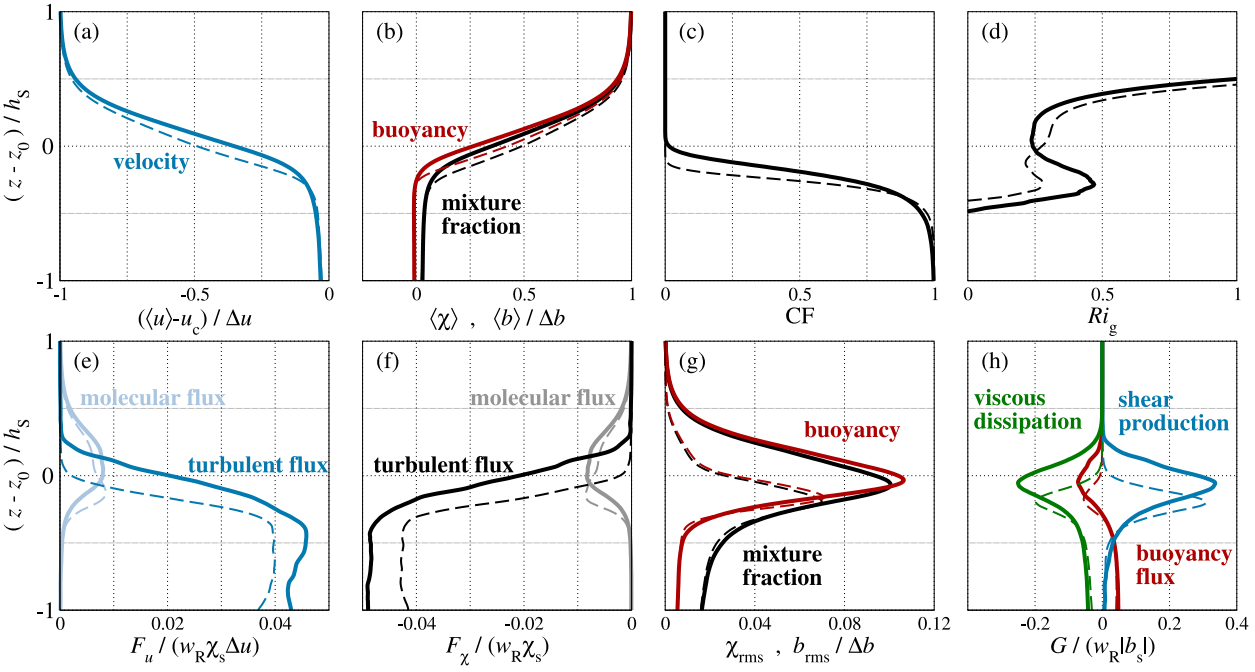

FIG. 7. Temporal evolution of the EIL vertical structure in case H11: (a) mean velocity (in a frame of reference moving with the cloud); (b) mean mixture fraction and buoyancy; (c) cloud fraction; (d) gradient Richardson number $\mathrm{Ri}_g = (\partial\langle b\rangle/\partial z)/(\partial\langle u\rangle/\partial z)^2$; (e) Reynolds stress $F_u = R_{uw} = \langle w'u'\rangle$ and molecular flux $F_u = -\nu\partial\langle u\rangle/\partial z$; (f) mixture fraction turbulent flux $F_\chi = \langle w'\chi'\rangle$ and molecular flux $F_\chi = -\kappa\partial\langle\chi\rangle/\partial z$; (g) mixture fraction and buoyancy root mean square (rms); and (h) budget of the turbulence kinetic energy, Eq. (12) with shear production rate $G = P$, buoyancy turbulent flux $G = B$, and viscous dissipation rate $G = -\varepsilon$. Dashed lines indicate the early time $t_1/t_R = 12.0$ and solid line corresponds to the final time $t_2/t_R = 27.1$.

the turbulent buoyancy flux, and $\tau'_{ij} = \nu(u'_{i,j} + u'_{j,i})$ is the fluctuating part of the viscous stress tensor. The profile of the shear production term in Fig. 7h clearly exposes a region of strong mechanical mixing: After a time interval $t_2 \simeq 27t_R$, shear production dominates approximately the lower half of the EIL and the profiles of viscous dissipation rate and buoyancy flux simply follow that of P. (See also Figs. 5c,d.) Henceforth, we will refer to this region as the turbulent EIL sublayer.

In sum, we can split the EIL into an upper, nonturbulent sublayer and a lower, turbulent sublayer. The turbulent, shear-dominated EIL sublayer acts as a transition region between the upper, nonturbulent part, a remnant of the initial and local dominant balance between the shear and the stable stratification, and the cloud layer, a free-convection zone where turbulence is sustained by the buoyancy reversal instability (Fig. 8).

The vertical position of the turbulent EIL sublayer $z_i(t)$ can be defined by the maximum in the vertical profile of the shear production term at any given time:

$$P[z_i(t), t] = \max_z [P(z, t)]. \tag{13}$$

An additional length scale

$$\delta = z_i - z_0 + h_S/2 \tag{14}$$

is introduced in Fig. 8. It is the distance between $z_i(t)$ and the base of the background shear layer at $z = z_0 - h_S/2$ and it measures the penetration depth associated with the encroachment of the in-cloud turbulence into the EIL. The corresponding mean entrainment velocity is

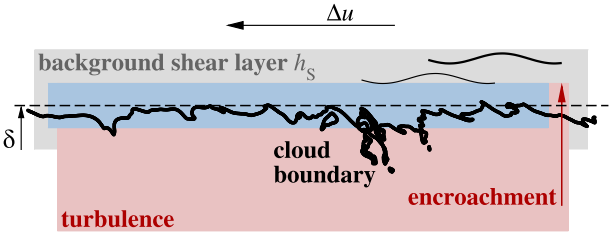

FIG. 8. Sketch representing the EIL vertical structure. The position of maximum shear provides the reference height z_i (dashed line) and the penetration depth δ [Eq. (14)] defines the relative position of the background shear layer (gray stripe, thickness h_S). The black jagged line is the cloud boundary. The blue stripe indicates the lower, turbulent EIL sublayer, where shear dominates the production of turbulence kinetic energy. Beneath the EIL, free convection dominates. Wavy lines at the top-right corner represent gravity waves.

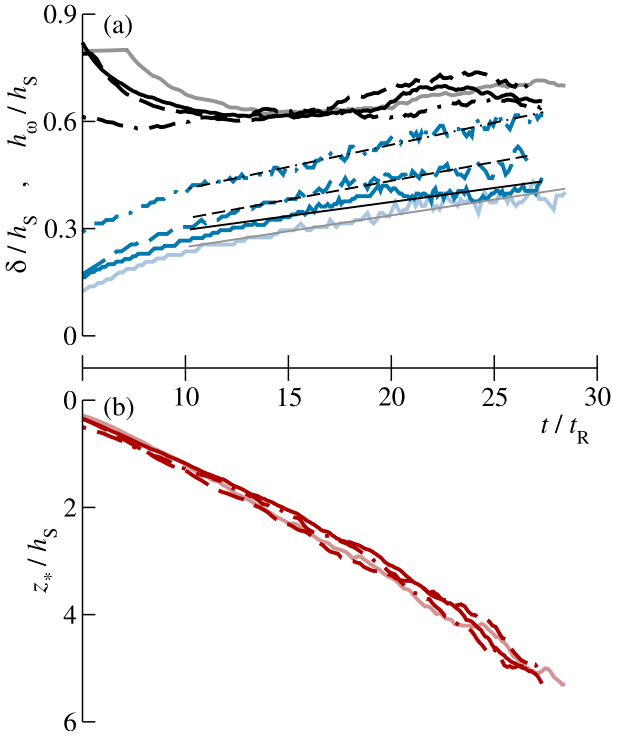

FIG. 9. Temporal evolution of the length scales (a) inside the EIL and (b) inside the cloud layer: black is vorticity thickness h_ω, blue is the penetration depth δ, and red is the convection scale z_*. Line styles: reference case H11 (solid), case M21 with twice the reversal strength D (dashed), and case M12 with twice the reversal interval χ_s (dotted–dashed). Light colors correspond to case M11 with half the Reynolds number Re_0 of case H11. Thin straight lines in (a) correspond to the model of $\delta(t)$ according to Eq. (15) and Eq. (21).

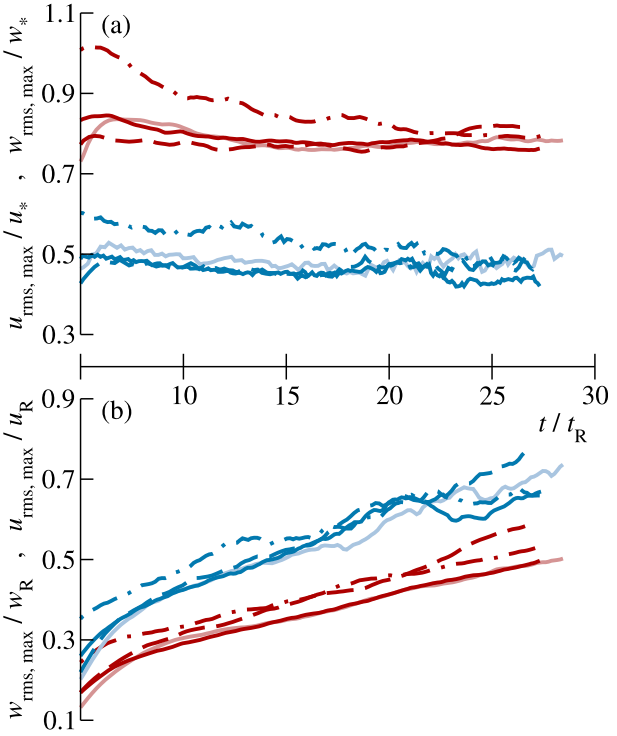

FIG. 10. Temporal evolution of the vertical (red) and horizontal (blue) velocity root-mean-square (rms) maxima $w_{\mathrm{rms}} = \langle w'w' \rangle^{1/2}$ and $u_{\mathrm{rms}} = \langle u'u' \rangle^{1/2}$, respectively. Values normalized (a) by the corresponding instantaneous velocity scales w_* and u_* and (b) by the reference scales w_R and u_R. Lines indicate the following: solid is the reference case H11, dashed is case M21 with twice the reversal strength D, and dotted–dashed is case M12 with twice the reversal interval χ_s. Light colors correspond to case M11 with half the Reynolds number Re_0 of case H11.

$$w_e = \frac{dz_i}{dt} = \frac{d\delta}{dt}. \tag{15}$$

The two main attributes regarding the evolution of this vertical structure are that (i) the EIL is characterized by a vorticity thickness $h_\omega(t) \simeq h_S$, where h_S is a constant defined by Eq. (6), and (ii) the in-cloud turbulence encroaches into the EIL slowly compared to the development of the convection layer inside the cloud. The first attribute was demonstrated with the help of Fig. 3, and the second attribute is shown in Fig. 9: During the time in which the turbulence has advanced only $\delta \simeq (1/5)h_S$ into the EIL, the convection length scale

$$z_* = (1/B_{\max}) \int_{-\infty}^{\infty} \max(B, 0)\, dz \tag{16}$$

characterizing the vertical size of the convection layer (Deardorff 1980; Mellado 2012) has become $\simeq 5h_S$, or 25 times larger. [The integrand $\max(B, 0)$ is used to retain solely the interval of the buoyancy flux profile contributing to the turbulence production.]

5. Turbulence velocity scales

A last intermediate step toward a parameterization for w_e consists in estimating the velocity scale u_* characterizing the mixing inside the turbulent EIL sublayer. As explained in this section, this velocity scale u_* can be obtained from the velocity scale w_* characterizing the in-cloud turbulence, which in turn relates the dependence of u_* on the parameters of the problem to that of the buoyancy reference scale w_R, introduced in section 3.

The prevalence of free-convection conditions inside the cloud suggests that the convection velocity

$$w_* = (B_{\max} z_*)^{1/3} \tag{17}$$

characterizes the in-cloud turbulence (Deardorff 1970). This argument is confirmed by Figs. 10a and 11b. In particular, the ratio between the maximum of the vertical velocity root mean square (rms), $w_{\mathrm{rms}} = \langle w'w' \rangle^{1/2}$, and w_* is of $O(1)$, approximately constant in time after an initial transient, and approximately independent of

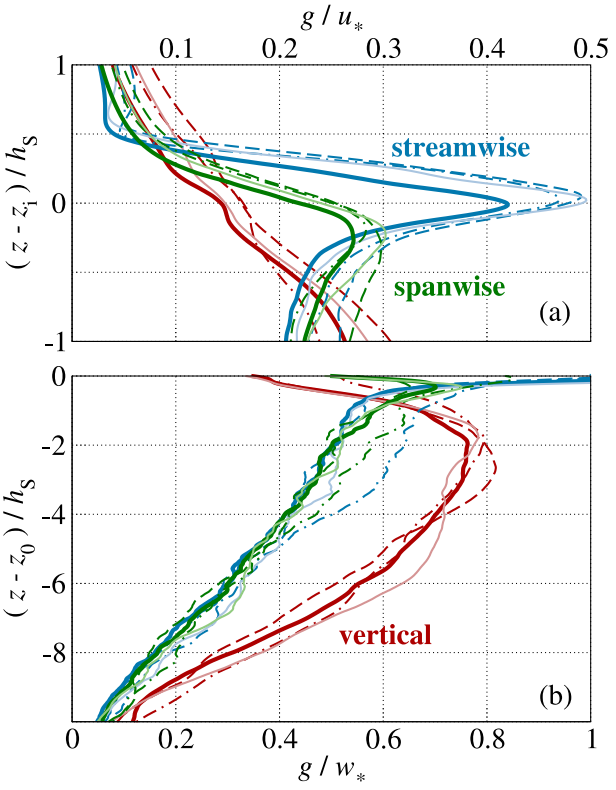

FIG. 11. Vertical profiles at the final times $t_2/t_R \simeq 27$ of the rms of the streamwise, spanwise, and vertical velocity components (a) inside the EIL and normalized by u_* [Eq. (18)] and (b) inside the cloud layer and normalized by w_* [Eq. (17)]. Solid line is the reference case H11, dashed line is case M21 with twice the reversal strength D, and dotted–dashed line is case M12 with twice the reversal interval χ_s. Light colors correspond to case M11 with half the Reynolds number Re_0 of case H11.

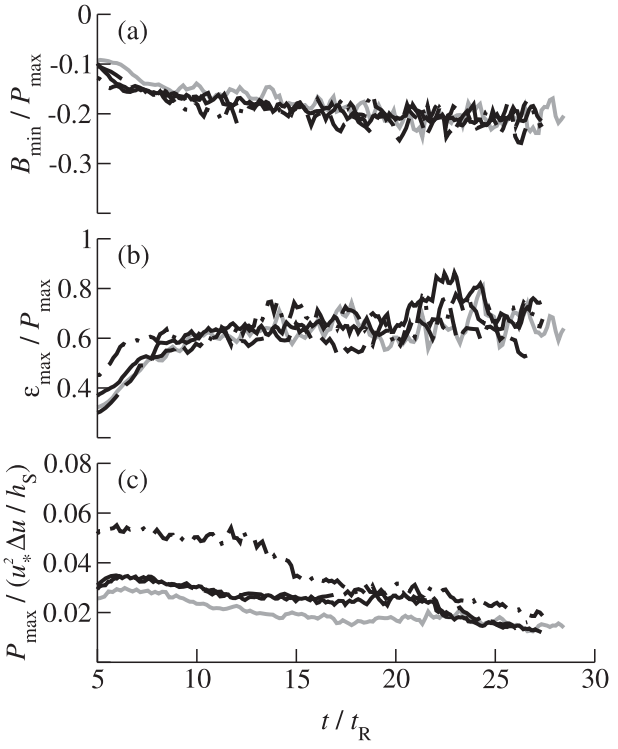

FIG. 12. Temporal evolution of the characteristic values of (top to bottom) the terms in the evolution equation for the turbulence kinetic energy [Eq. (12)] inside the EIL turbulent sublayer (Fig. 7h). Solid line is the reference case H11, dashed line is case M21 with twice the reversal strength D, and dotted–dashed line is case M12 with twice the reversal interval χ_s. Gray color corresponds to case M11 with half the Reynolds number Re_0 of case H11.

the buoyancy reversal parameters, χ_s and D, and the reference Reynolds number Re_0 (approximately in the sense that variations of 100% in these parameters lead to variations in normalized velocity rms of 10% or less beyond $\simeq 15 t_R$).

In contrast, shear (instead of free convection) dominates the turbulent EIL sublayer and the shear Reynolds stress R_{uw} (instead of the buoyancy flux) becomes the relevant term for turbulence production inside this sublayer. Mechanistically, we can argue that the shear Reynolds stress scales according to $R_{uw} \sim w_* \delta\, (\Delta u/h_S)$, on the basis that a vertical velocity fluctuation proportional to w_* is associated with a horizontal velocity fluctuation $\delta\, (\Delta u/h_S)$ caused by the displacement δ over a background shear $\Delta u/h_S$. [The factor $\simeq 3/2$ discussed in section 4 is of $O(1)$ and therefore neglected for the estimate of the parametric dependence pursued here.] Hence, from the relation $R_{uw} \sim u_*^2$ expressing the Reynolds stress in terms of a velocity scale u_*, we can expect that

$$u_* = [w_* \delta (\Delta u/h_S)]^{1/2} \tag{18}$$

characterizes the turbulence velocity fluctuations inside the EIL. This is confirmed by the approximate steady behavior of u_{rms}/u_* and the collapse of the curves for the different cases observed in Figs. 10a and 11a, at least within the statistical convergence achieved with our simulations.

We are interested in a parameterization for u_*, either directly or, according to Eq. (18), indirectly through a parameterization of w_* and δ. Appendix A shows that δ can be related to w_* so that, actually, we only need to obtain the functional relation $w_* = \Delta u f(D, \chi_s; t/t_R)$. A substantial part of the parametric dependence of w_* on the buoyancy reversal parameters D and χ_s is captured by the buoyancy reversal scale $w_R = \Delta u \sqrt{D/3}$ [Eq. (10)]. This is shown by the ratios w_{rms}/w_R of order one in Fig. 10b, the different curves approximately collapsing on top of each other, and it is consistent with the physical interpretation of w_R provided in section 3. The velocity scale w_R does not include the temporal dependence of w_* on t/t_R but it provides the correct order of magnitude of the in-cloud

turbulence intensity, which is the purpose of introducing w_R within this context. Concomitantly, an estimate u_R for the velocity rms inside the turbulent EIL sublayer is

$$u_R = (w_R \chi_c \Delta u)^{1/2} = [\chi_c (D/3)^{1/2}]^{1/2} \Delta u. \qquad (19)$$

This scale is obtained from Eq. (18) by substituting w_* by w_R and δ by $\chi_c h_S$—the extent of the background shear layer that is convectively unstable. Figure 10b supports this definition, since it again yields ratios $u_{\rm rms}/u_R$ of order one that are approximately common to all the cases.

We note again that the reference scales w_R and u_R do not retain the nearly linear growth in time of w_* and u_* deduced from Fig. 10b, but we introduce them here because they provide readily the dependence of the turbulence intensities on the parameters of the problem both inside the cloud and inside the EIL, which proves useful in the discussion that follows.

6. Mean entrainment velocity

A parameterization for the mean entrainment velocity, in our case $w_e/\Delta u = f(D, \chi_s; t/t_R)$, is often based on the analysis of the evolution equation for the mean buoyancy. Appendix B explains that the two dominant terms in that equation are the contribution from the distortion of the mean buoyancy profile and the contribution from the turbulent flux. Statistical convergence is insufficient to ascertain if these two terms scale with one another and to obtain a possible dependence on time of w_e. Therefore, we try to identify first the parametric dependence $w_e/\Delta u = f(D, \chi_s)$ based on the relation $w_e \Delta b \sim B_{\rm min}$. This choice is also justified by the observation in Fig. 9 that $\delta(t)$ can be reasonably well approximated by a linear growth in time.

First, we hypothesize

$$w_e \Delta b \sim P_{\rm max} \qquad (20)$$

based on the following observations regarding the evolution equation for the turbulence kinetic energy e, Eq. (12): (i) $B_{\rm min}/P_{\rm max}$ and $\varepsilon_{\rm max}/P_{\rm max}$ are approximately constant and of order one (Figs. 12a,b), (ii) the turbulent transport term (not shown) is $\simeq$10% of $P_{\rm max}$ and therefore negligible to leading order, and (iii) the time rate of change of e is also negligibly small compared to $P_{\rm max}$, as inferred from Fig. 12 by adding the buoyancy flux and the viscous dissipation terms. [It is interesting to note that the resulting dominant balance $P \simeq -B + \varepsilon$ and flux Richardson number $-B/P \simeq 0.2$ coincide with those found in cloud-free, sheared interfacial layers for stratification conditions $z_* \Delta b/(\Delta u)^2 \simeq 1-2$, comparable to those explored here, despite the different turbulence forcing mechanism (Strang and Fernando 2001).]

Second, the behavior inside the EIL just described is also similar to that found in cloud-free, stably stratified homogeneous turbulence (see, e.g., Chung and Matheou 2012 and references therein), with a turbulence kinetic energy proportional to u_*^2 (Figs. 10a and 11a) and with a background mean shear proportional to $(\partial\langle u\rangle/\partial z)_{\rm max} = \Delta u/h_\omega \simeq \Delta u/h_S$ (Fig. 9). Accordingly, $u_*^2 \Delta u/h_S$ captures a large part of the evolution and parametric dependence of $P_{\rm max}$, as seen in Fig. 12c.

As a consequence of the above it follows that a first estimate for the mean entrainment velocity is $w_e \sim P_0/\Delta b$, as anticipated by Eq. (11), where the reference shear production rate $P_0 = u_R^2(\Delta u/h_S) = \chi_c \sqrt{3D} \Delta b \Delta u$ provides an estimate of $P_{\rm max} \sim (u_*/u_R)^2 P_0$, on the basis that u_R provides an estimate for u_* (section 5). This last step finally yields the parameterization

$$w_e \simeq c_1 \chi_c \sqrt{3D} \Delta u. \qquad (21)$$

Note that the direct dependence on Δb drops out of this relation because it affects the system in two different ways that compensate each other: On the one hand, it diminishes w_e as the stratification increases; on the other hand, for a given Δu, it also diminishes the inversion thickness h_S such that the shear, and thus the shear production rate P_0 and ultimately the turbulent buoyancy flux, augments in the same amount. However, Δb still influences w_e indirectly through D—the relative strength of evaporative cooling defined by Eq. (3).

The coefficients c_1 in Eq. (21) for the different cases (Table 1) are obtained from the corresponding evolution of $\delta(t)/h_S$, which is plotted in Fig. 9 (only data beyond $t/t_R \simeq 10$ has been used in the linear regression analysis). The variation of $\simeq 50\%$ in c_1 for the case M21 when D is increased by a factor of 2 with respect to the reference case indicates that the parameterization of the dependence on D could be improved. Nonetheless, this uncertainty affects the parametric dependence but not the magnitude of w_e, and this level of accuracy and understanding of the problem is enough to address the questions stated in the introduction.

The first question to be addressed is how much can the wind shear enhance the mean entrainment velocity caused by buoyancy reversal. Data from the simulation H11 and Eq. (21) lead to $w_e \simeq 0.82 \times 10^{-3} \Delta u$. Because the dependence on the Reynolds number Re_0 has been observed to be relatively small in all the figures (Reynolds number similarity), we can apply this relation to the RF01/DYCOMS II case, where $\Delta u = 3.8\,\mathrm{m\,s^{-1}}$, and we obtain $w_e \simeq 3\,\mathrm{mm\,s^{-1}}$. This result has two important implications:

(i) This value is an order of magnitude larger than that found in shear-free conditions, where buoyancy reversal alone can only explain an entrainment

velocity $\simeq 0.2\,\mathrm{mm\,s^{-1}}$ and an inversion thickness $\simeq 0.1\,\mathrm{m}$ (Mellado et al. 2010).

(ii) This value is comparable with the measurements, in particular, with the velocity $3.8 \pm 1\,\mathrm{mm\,s^{-1}}$ reported in the RF01/DYCOMS II case (Stevens et al. 2003b), and, in general, with the interval $2-5\,\mathrm{mm\,s^{-1}}$ measured in that field campaign (Faloona et al. 2005).

Hence, high enough wind shear can render buoyancy reversal comparable to other forcing mechanisms operative within the EIL. Additional processes in the real case will likely modify the observed entrainment rates. For instance, longwave radiative cooling can increase w_* and thereby the penetration depth δ and the entrainment velocity w_e. Also, an initial offset between the centers of the shear and the inversion layers might alter the mixing process (Carpenter et al. 2007). Another aspect to consider is the effect of detailed microphysics on w_e, like the gravitational settling or the finite evaporation rate, although the strong mixing caused by the wind shear is expected to limit the corresponding reduction in w_e observed in shear-free conditions (de Lozar and Mellado 2014). Notwithstanding these and possibly other open questions that still remain to be addressed, the enhancement of entrainment rate found in this analysis clearly demonstrates that mean shear can play a key role in the cloud-top region of the STBL and deserves further analysis than it has received so far.

7. Discussion

This section discusses further some aspects of the problem within the context of the STBL and it is organized around two topics: (i) the relevance of the strong-shear regime considered in this paper and the anticipation of a second regime for ratios $w_{\mathrm{rms}}/\Delta u \gtrsim 1$, and (ii) the implications of the results for the concept of the cloud-top entrainment instability.

The extension of the results presented so far to velocity differences larger than those specifically used in the simulations ($\Delta u = 0.5-0.6\,\mathrm{m\,s^{-1}}$; Table 1) relies on the property of Reynolds number similarity anticipated in the introduction and observed in several figures throughout the paper, where the curves from cases H11 and M11 with a factor-of-2 different Reynolds numbers collapse approximately on top of each other. This behavior is consistent with that documented in other turbulent flows for outer-scale Reynolds numbers beyond $O(10^4)$ [e.g., see review by Dimotakis (2000)], since the characteristic Reynolds numbers achieved in the reference simulation H11 are $w_* z_*/\nu \simeq 5.6 \times 10^3$ (in-cloud turbulence) and $u_* h_S/\nu \simeq 1.7 \times 10^3$ (EIL turbulence).

a. Time scales and regimes

There are three time scales that are relevant for the description of the evolution of the system: t_S, given by Eq. (8); t_R, given by Eq. (9); and h_S/w_e. The proportions among these time scales are $1: 1/\sqrt{D/3} : [1/(c_3\chi_c)](1/\sqrt{D/3})$. Hence, the typical atmospheric conditions $D \ll 1$ and $\chi_c \ll 1$ imply a separation of scales $t_S \ll t_R \ll h_S/w_e$ that allows us to distinguish different phases of development, or regimes.

The first time scale provides an estimate, about 10 t_S according to Fig. 3, for how long the mean shear requires to create a background shear layer of thickness h_S and with decaying turbulence inside of it (Fig. 4).

The second time scale provides an estimate, about 10 t_R according to Fig. 9 and Fig. 10, for how long buoyancy reversal needs to establish the regime considered here—namely, a turbulent convection layer with a turbulence intensity of the order of w_R, which satisfies $w_R \ll \Delta u$, and encroaching into a relatively flat EIL (Fig. 5).

The third time scale h_S/w_e indicates how long that regime can exist before the background shear layer is consumed and we start to observe undulations of the EIL. Such a transition of regimes is often discussed in terms of an internal Richardson number $\mathrm{Ri}_{(I)}$ that compares the thickness of the background density interfacial layer—the thickness h_S of the background shear layer in the current problem—with a vertical displacement $w_*^2/\Delta b$ associated to the turbulence kinetic energy at one side of that density interfacial layer—here, the turbulence kinetic energy inside the cloud layer (see Fernando and Hunt 1997 and references therein). When $\mathrm{Ri}_{(I)}$is large enough, the EIL remains flat and is sufficiently thick to support gravity waves inside of it. When $\mathrm{Ri}_{(I)}$ is small enough, undulations with an amplitude larger than h_S form, and the EIL is no longer flat but convoluted. In the cases analyzed here, $\mathrm{Ri}_{(I)}$ is commensurate with $(w_*/\Delta u)^{-2}$, according to its definition $\mathrm{Ri}_{(I)} = h_S \Delta b/w_*^2$ and Eq. (6). Hence, $\mathrm{Ri}_{(I)}$ is initially large because $w_*/\Delta u \ll 1$ but it keeps decreasing as the in-cloud turbulence intensity increases, and eventually we will enter into the aforementioned second regime. This second regime, as well as the transition into it when w_* becomes comparable to Δu, is as interesting as the first regime considered in this paper, but more difficult to access numerically, and so it is deferred to future work.

Particularized to the reference case RF01/DYCOMS II, the increments $\Delta u = 3.8\,\mathrm{m\,s^{-1}}$ and $\Delta b \simeq 0.25\,\mathrm{m\,s^{-2}}$ imply a background shear layer forming in about 1–2 min ($10 t_S \simeq 50\,\mathrm{s}$). We have $t_R \simeq 49\,\mathrm{s}$, so that in 5–10 min we would obtain a turbulent layer advancing into that background shear layer and establishing the EIL structure sketched in Fig. 8 and illustrated in Fig. 5. This

encroachment process would last for about $h_S/w_e \simeq 1$–2 h before all the remnant of the background shear layer inside the upper part of the EIL is consumed. Since these three time scales are relatively well separated, it is reasonable that mean-shear effects as discussed in this paper reproduce or explain part of the observations.

For instance, regarding the vertical structure, the predicted depth is $h_S \simeq 20$ m, which is comparable to the interval 20–80 m reported by Faloona et al. (2005). Also, the relatively moist and cold smooth transition from the cloud-top boundary to the free troposphere aloft seen in Figs. 5 and 7, with a relatively sharp inversion base and a less marked upper boundary, agrees well with STBL data (Caughey et al. 1982; Moeng et al. 2005; Haman et al. 2007; Kurowski et al. 2009; Wood 2012). Equally, we can identify the turbulent EIL sublayer with the turbulent inversion (sub)layer reported sometimes in field measurements (Katzwinkel et al. 2012; Malinowski et al. 2013). Regarding the turbulence intensities, our analysis indicates that buoyancy reversal leads to $w_{\rm rms} = 0.2\,{\rm m\,s^{-1}}$ inside the cloud after $\simeq$20 min. Although this velocity rms starts to be comparable with the in-cloud values $\simeq 0.6\,{\rm m\,s^{-1}}$ reported in Stevens et al. (2003b), it is still smaller by a factor of 3, which indicates that other turbulence sources not retained here, like radiative cooling, are still dominant. This argument also helps to explain that h_S lies in the lower end of the measurement interval of EIL thicknesses, since more intense turbulence would promote additional mixing and thus a thicker EIL. In contrast, the entrainment velocity $\simeq 3\,{\rm mm\,s^{-1}}$ found in our analysis is already comparable to those inferred from the measurements, of the order of 2–5 $\rm mm\,s^{-1}$ (Stevens et al. 2003b; Faloona et al. 2005). This contrast suggests that shear effects can remain very localized at the EIL without affecting the in-cloud turbulence as much as they affect the EIL properties, at least when considered in its interaction with buoyancy reversal.

Last, it is noted that buoyancy reversal conditions, $D > 0$, and not only evaporative cooling conditions $-\chi_s < D$ are necessary for turbulence generation and therefore a nonzero entrainment velocity, at least in the absence of radiative cooling. In other words, Eq. (21) has to be substituted by $w_e = 0$ for $D < 0$. The reason is that the condition $D \leq 0$ leads merely to a self-limiting stably stratified EIL where turbulence is not maintained (section 3). This limitation of evaporative cooling effects, however, might be different when other mechanisms of turbulence generation, like radiative cooling, are present.

b. Cloud-top entrainment instability

As briefly reviewed during the introduction, the buoyancy reversal condition $D > 0$ (or a similar inequality involving just thermodynamic properties) has been found in recent work to be obviously necessary but not sufficient for a cloud breakup to occur: Buoyancy reversal alone is diffusion limited and too weak, and the corresponding mixing rate is one order of magnitude smaller than what is observed in measurements (Mellado 2010).

In combination with the local wind shear at the EIL, we have demonstrated in this paper that evaporative cooling might become as strong as other processes and therefore might play a nonnegligible role in cloud desiccation and in the transition from the stratocumulus regime to the shallow-cumulus regime. However,

(i) We still do not observe a runaway instability in the sense of a divergence of some statistical measure in a finite time. The entrainment velocity $w_{\underline{e}}$ is relatively large but remains approximately constant in the regime $w_* \ll \Delta u$ studied in this paper.

(ii) The parameterization (21) shows that w_e depends crucially on the velocity difference Δu and not only on the presence of buoyancy reversal conditions, $D > 0$. The mean wind shear always acts as a catalyst of turbulence driven by buoyancy reversal, but a relatively large Δu is necessary to generate thereby turbulence intensities and entrainment velocities comparable to those caused by radiative cooling. In particular, the shear associated with the convective motions inside of the STBL, with typical values $\Delta u \simeq 1\,{\rm m\,s^{-1}}$, is insufficient to explain the observed levels of in-cloud turbulence by means of buoyancy reversal effects solely. For instance, for the RF01/DYCOMS II case, such velocity differences would imply $w_{\underline{e}} \simeq 0.8\,{\rm mm\,s^{-1}}$, which is more than a factor of 4 smaller than the measurements.

(iii) The reduction of Δb for stratocumulus in the tropical regions as the cloud deck is advected into a warmer ocean surface, assuming a constant Δu, tends to increase the thickness of the inversion as $h_{\underline{S}} \propto (\Delta b)^{-1}$ and hence to dilute the cloud top: This dilution occurs even without buoyancy reversal. (Although, at the same time, the corresponding time scales increase proportionally and it might then be that mean-shear effects become simply too slow and other forcing mechanism dominate the transition toward the shallow-cumulus regime.)

8. Conclusions

The interaction between buoyancy reversal and a mean vertical shear localized at the entrainment interfacial layer of the STBL has been investigated by means of direct numerical simulations. The physical

model, the cloud-top mixing layer, retains the effect of the buoyancy and velocity increments across the inversion, Δb and Δu, and the effect of the buoyancy reversal parameters, D and χ_s. Dimensional analysis allows us to reduce the problem to just the last two parameters, once the Reynolds number drops out of the analysis on the basis of the observed Reynolds number similarity (the Prandtl number is set to one).

The EIL structure is determined first by the balance between the mean shear and the mean stratification. The resulting background shear layer with decaying turbulence has been documented extensively in the past for similar cloud-free configurations based on laboratory work and numerical simulations, and provides the reference thickness $h_S = (1/3)(\Delta u)^2/\Delta b$. We have argued that it forms relatively fast, in a time scale $\simeq 10\Delta u/\Delta b$, so that h_S consistently predicts the lower bound of the EIL thickness measured in the STBL under shear conditions. Other processes modify this background shear layer and we have considered in this paper the effect of buoyancy reversal.

In the regime of strong shear considered in this paper (i.e., the case in which Δu is larger than the characteristic velocity fluctuation of the in-cloud turbulence), the EIL remains flat, with a thickness comparable to h_S, and the EIL can be split into two sublayers. The upper, quasi-laminar EIL sublayer is a relatively moist and cold region that provides a smooth transition between the cloud-top and the free troposphere, which is in agreement with available STBL data. In contrast, the lower, turbulent EIL sublayer is characterized by strong mechanical mixing. All of the shear production concentrates in this relatively thin turbulent EIL sublayer and the mean shear inside the cloud core remains negligibly small.

We find that the combination of a relatively strong shear with buoyancy reversal can lead to entrainment rates comparable to those believed to be caused by other sources of convective instability—for instance, cloud-top radiative cooling. We have provided the following parameterizations to assess the occurrence of this situation: The velocity rms is well characterized by $w_R = \sqrt{D/3}\Delta u$ inside the cloud layer and by $u_R = \sqrt{\chi_c}(D/3)^{1/2}\Delta u$ inside the turbulent EIL sublayer, where $\chi_c = (\chi_s + D)/(1 + D)$ bounds the interval of mixtures that are negatively buoyant. Both velocity scales are related by the observed encroachment of the turbulence into the upper EIL sublayer as the in-cloud turbulence intensifies. The point of maximum shear production is used to track this encroachment and the associated mean entrainment velocity is well parameterized by $w_e \simeq 0.02\chi_c\sqrt{3D}\Delta u$. The time scales that define the establishment and duration of the regime of strong shear considered in this paper are $10t_R$ and $h_S/w_e \simeq [1/(0.03\chi_c)]t_R$, respectively, where $t_R = (1/\sqrt{3D})\Delta u/\Delta b$. For typical atmospheric conditions, $10t_R \ll h_S/w_e$—a scale separation that supports the relevance of this regime and thus the appropriateness of the current study.

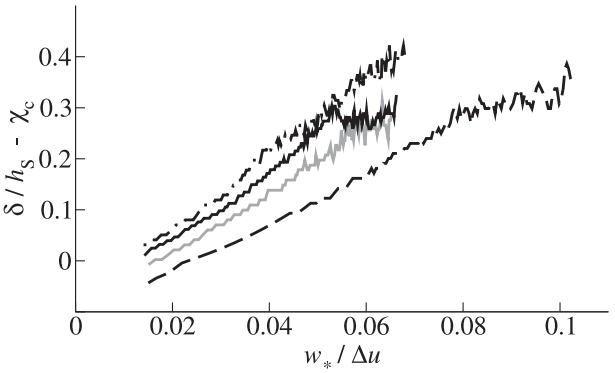

FIG. A1. Temporal evolution of the penetration depth δ as a function of the convection velocity w_* in Eq. (A1). Solid line is case H11, dashed line is case M21, and dotted–dashed line is case M12. Light colors correspond to case M11 with half the Reynolds number Re_0 of case H11.

The mixing rate, as measured by w_e, remains finite (approximately constant in the regime considered in this work) and there is no indication of a runaway instability leading to a rapid desiccation of the cloud. Further work on the second regime, in which the in-cloud velocity rms becomes comparable to Δu and the EIL develops undulations instead of being relatively flat, could be helpful to further assess the possible existence of a cloud-top entrainment instability. Note, however, that this process depends crucially on the interaction of evaporative cooling with other mechanisms and not only on the necessary condition $D > 0$ (or equivalent), as proved in this paper.

Based on these results and the corresponding analysis presented throughout the paper, we believe that processes controlling the mean shear at the inversion are likely critical to the dynamics of the stratocumulus-topped boundary layer, and merit more attention than they have received in the literature to date.

Acknowledgments. Fruitful discussions with S. Malinowski, S. Sarkar, J. Schumacher, and R. Shaw are gratefully acknowledged. Partial financial support was provided by the Deutsche Forschungsgemeinschaft, SPP 1276 Metström program. Computational time was provided by the German Climate Computing Center in Hamburg and by the Jülich Supercomputing Centre. This research was supported in part by the National Science Foundation under Grant NSF PHY05-51164 and we thank the

kind hospitality of the Kavli Institute for Theoretical Physics.

APPENDIX A

Penetration Depth

The length scale δ defined by Eq. (14) constitutes a penetration depth or buoyancy length scale as introduced before in the literature for similar configurations. Given a vertical velocity w', the vertical displacement associated with it inside a linearly stratified region is proportional to w'/N, where N is the buoyancy frequency of the stratified background (e.g., Smyth and Moum 2000, Chung and Matheou 2012, and references therein). Identifying w' and N^2 in this model with w_* and $\Delta b/h_S$ in our problem leads to

$$\delta/h_S = \chi_c + c_2 + c_3 w_*/\Delta u, \tag{A1}$$

where the convection velocity w_* [Eq. (17)] provides an estimate of the intensity of in-cloud turbulence (section 5). This linear relation is strongly supported by Fig. A1. The slopes for the different cases are summarized in Table 1, the mean value being $c_3 \simeq 6$ (only data beyond $w_*/\Delta u \simeq 0.02$ has been used in the linear regression). The observed dependence of c_3 on D and χ_s, which leads to a variation of about 25% with respect to the reference case H11, is not clear, although we might argue that it is small considering that those two control parameters change by a factor of 2 in cases M21 and M12, respectively, with respect to H11. [The first term in the right-hand side of Eq. (A1) takes into account the fact that the lower part of the background inversion, of size commensurate with $\chi_c h_S$, is convectively unstable and falls down independently of having a mechanical forcing (here represented by w_*) or not.]

This result, though not needed for the derivation of an estimate of the mean entrainment velocity, is important for several reasons. First, the relation $\delta \propto w_*(h_S/\Delta u)$ implied by Eq. (A1), along with Eq. (18), leads to $u_* \propto w_*$ and thereby a series of consistency results: (i) Eq. (18) can be written as $u_* \propto \delta\,(\Delta u/h_S)$—a result typical of homogeneous shear turbulence if δ is interpreted as the local integral scale and $\Delta u/h_S$ as the mean shear. [However, the scaling $u_* \simeq \delta\,(\Delta u/h_S)$ alone fails to capture the observed dependence of $w_{\mathrm{rms,max}}/u_{\mathrm{rms,max}}$ on χ_s and D, which is the motivation for the somewhat more elaborated definition (18).] (ii) The penetration length δ is proportional to the corresponding Ozmidov scale $[\varepsilon/(\Delta b/h_S)^{3/2}]^{1/2}$, which in general characterizes the maximum size of the turbulent motions that are allowed by a strong enough stratification (e.g., Smyth and Moum 2000, Chung and Matheou 2012, and references therein).

Second, Eq. (A1) shows that the measurement of the in-cloud turbulence intensity or w_* would be enough to infer a large amount of information about the system (cf. Fig. 8), even $w_e = d\delta/dt$ if the time rate of change dw_*/dt can be measured. This relation implies that the entrainment velocity is characterized by w_*, to leading order, and the buoyancy reversal enters only indirectly through w_* or as second-order deviations (the small dependence of c_3 on D and χ_s indicated before). It would be interesting to see in future work if, consistently, a relation similar to Eq. (A1) is found when longwave radiative cooling determines most of the in-cloud turbulence intensity w_*.

APPENDIX B

Mean Entrainment Velocity

The mean entrainment velocity $w_e \equiv dz_i/dt$ is often written as the sum of a turbulent and nonturbulent contribution (Stevens 2002; Wood 2012)

$$w_e = w_{e,t} + w_{e,n}. \tag{B1}$$

Integrating vertically the transport equation for the mean buoyancy deviation $\Delta b - \langle b\rangle$ from z_i upward provides an expression for each of those contributions:

$$\begin{aligned} w_{e,t} &\equiv -\frac{\langle b'w'\rangle[z_i(t),t]}{\Delta b - \langle b\rangle[z_i(t),t]} \\ w_{e,n} &\equiv \frac{1}{\Delta b - \langle b\rangle[z_i(t),t]}\left\{\kappa\frac{\partial\langle b\rangle}{\partial z}[z_i(t),t]\right. \\ &\quad \left. -\frac{d}{dt}\left[\int_{z_i(t)}^{\infty}(\Delta b - \langle b\rangle)\,dz\right] - \int_{z_i(t)}^{\infty}\langle S\rangle\,dz\right\}. \end{aligned} \tag{B2}$$

A similar equation can be written based on the conserved scalar χ, in which case the contribution from the source term $S = -\kappa|\nabla\chi|^2 d^2b^e/d^2\chi^2$ does not appear. The choice of one scalar variable or the other, as well as the point $z_i(t)$ used as reference, is, to certain extent, arbitrary. For instance, it might be chosen based on some feature of a relevant physical property, like the mean position of the cloud boundary (a sharp variation of the condensate mass fraction) or the mean position of the turbulence interface (a sharp variation of the enstrophy); it might also be chosen so that the terms in the equation above are easiest to measure, or it might be chosen such that as many terms as possible in the equation above are negligible. However, once we have agreed upon it, the relations above hold and

the derivation that follows should reflect that choice consistently.

The particular choice of z_i used in this paper, Eq. (13), is motivated, first, by the relevance of the shear production term in the dynamics of the EIL (section 4), and, second, by the clear signature of the shear production term inside the EIL and the concurrence of the maxima of the production rate, the viscous dissipation rate and the horizontal velocity rms, and the minimum turbulent buoyancy flux (Figs. 7h and 11).

Analysis of the data from case H11 shows that all of the contributions to w_e in the equation above are positive and their magnitudes, compared to that of the turbulent flux, are as follows: (i) the relative contribution from the source term is $\simeq$0.3, slightly decreasing in time (only $\simeq$10% of all the evaporative cooling $\int\langle S\rangle\, dz$ occurs above z_i); (ii) the relative contribution from the molecular term is 0.35, also decreasing in time; (iii) the relative contribution from the distortion or shape term is $\simeq$(1–1.5), which is the largest of the three terms but comparable to the turbulent flux for the turbulence regime considered in this work (cf. section 7). The buoyancy difference in the denominator is $\simeq$0.8, slightly decreasing. Hence, we can estimate $w_e \propto B_{\min}/\Delta b$ to leading order, as used in section 6.

REFERENCES

Abma, D., T. Heus, and J. P. Mellado, 2013: Direct numerical simulation of evaporative cooling at the lateral boundary of shallow cumulus clouds. *J. Atmos. Sci.,* **70,** 2088–2102.

Bretherton, C. S., 1987: A theory for nonprecipitating moist convection between two parallel plates. Part I: Thermodynamics and linear solutions. *J. Atmos. Sci.,* **44,** 1809–1827.

Brucker, K. A., and S. Sarkar, 2007: Evolution of an initially turbulent stratified shear layer. *Phys. Fluids,* **19,** 105105, doi:10.1063/1.2756581.

Carpenter, J. R., G. A. Lawrence, and W. D. Smyth, 2007: Evolution and mixing of asymmetric Holmboe instabilities. *J. Fluid Mech.,* **582,** 103–132.

Carpenter, M. H., and C. A. Kennedy, 1994: Fourth-order 2N-storage Runge-Kutta schemes. NASA Tech. Memo. TM-109112, 24 pp.

Caughey, S. J., B. A. Crease, and W. T. Roach, 1982: A field study of nocturnal stratocumulus II. Turbulence structure and entrainment. *Quart. J. Roy. Meteor. Soc.,* **108,** 125–144.

Chung, D., and G. Matheou, 2012: Direct numerical simulation of stationary homogeneous stratified sheared turbulence. *J. Fluid Mech.,* **696,** 434–467.

Conzemius, R., and E. Fedorovich, 2007: Bulk models in the sheared convective boundary layer: Evaluation through large eddy simulations. *J. Atmos. Sci.,* **64,** 786–807.

Deardorff, J. W., 1970: Convective velocity and temperature scales for the unstable planetary boundary layer and for Rayleigh convection. *J. Atmos. Sci.,* **27,** 1211–1213.

——, 1980: Cloud top entrainment instability. *J. Atmos. Sci.,* **37,** 131–147.

de Lozar, A., and J. P. Mellado, 2013: Direct numerical simulations of a smoke cloud-top mixing layer as a model for stratocumuli. *J. Atmos. Sci.,* **70,** 2356–2375.

——, and ——, 2014: Cloud droplets in a bulk formulation and its application for the buoyancy reversal instability. *Quart. J. Roy. Meteor. Soc.,* doi:10.1002/qj.2234, in press.

de Roode, S. R., and Q. Wang, 2007: Do stratocumulus clouds detrain? FIRE I data revisited. *Bound.-Layer Meteor.,* **122,** 479–491.

Dimotakis, P. E., 2000: The mixing transition in turbulent flows. *J. Fluid Mech.,* **409,** 69–98.

Faloona, I., and Coauthors, 2005: Observations of entrainment in eastern Pacific marine stratocumulus using three conserved scalars. *J. Atmos. Sci.,* **62,** 3268–3284.

Fernando, H. J. S., 1991: Turbulent mixing in stratified fluids. *Annu. Rev. Fluid Mech.,* **23,** 455–493.

——, and J. C. R. Hunt, 1997: Turbulence, waves and mixing at shear-free density interfaces. Part 1. A theoretical model. *J. Fluid Mech.,* **347,** 197–234.

Haman, K. E., S. P. Malinowski, M. J. Kurowski, H. Gerber, and J.-L. Brenguier, 2007: Small-scale mixing processes at the top of a marine stratocumulus—A case study. *Quart. J. Roy. Meteor. Soc.,* **133,** 213–226.

Katzwinkel, J., H. Siebert, and R. Shaw, 2012: Observation of self-limiting, shear-induced turbulent inversion layer above marine stratocumulus. *Bound.-Layer Meteor.,* **145,** 131–143.

Kurowski, M. J., S. P. Malinowski, and W. Grabowski, 2009: A numerical investigation of entrainment and transport within a stratocumulus-topped boundary layer. *Quart. J. Roy. Meteor. Soc.,* **135,** 77–92.

Lele, S. K., 1992: Compact finite difference schemes with spectral-like resolution. *J. Comput. Phys.,* **103,** 16–42.

Malinowski, S. P., and Coauthors, 2013: Physics of stratocumulus top (post): turbulence mixing across the capping inversion. *Atmos. Chem. Phys.,* **13,** 15 234–15 269.

Mashayek, A., and W. R. Peltier, 2011: Turbulence transition in stratified atmospheric and oceanic shear flows: Reynolds and Prandtl number controls upon the mechanism. *Geophys. Res. Lett.,* **38,** L16612, doi:10.1029/2011GL048542.

Mellado, J. P., 2010: The evaporatively-driven cloud-top mixing layer. *J. Fluid Mech.,* **660,** 5–36.

——, 2012: Direct numerical simulation of free convection over a heated plate. *J. Fluid Mech.,* **712,** 418–450.

——, and C. Ansorge, 2012: Factorization of the Fourier transform of the pressure-Poisson equation using finite differences in colocated grids. *Z. Angew. Math. Mech.,* **92,** 380–392.

——, B. Stevens, H. Schmidt, and N. Peters, 2009: Buoyancy reversal in cloud-top mixing layers. *Quart. J. Roy. Meteor. Soc.,* **135,** 963–978.

——, ——, ——, and ——, 2010: Two-fluid formulation of the cloud-top mixing layer for direct numerical simulation. *Theor. Comput. Fluid Dyn.,* **24,** 511–536.

Moeng, C.-H., B. Stevens, and P. P. Sullivan, 2005: Where is the interface of the stratocumulus-topped PBL. *J. Atmos. Sci.,* **62,** 2626–2631.

Moin, P., and K. Mahesh, 1998: Direct numerical simulation: A tool in turbulence research. *Annu. Rev. Fluid Mech.,* **30,** 539–578.

Monin, A. S., and A. M. Yaglom, 2007: *Statistical Fluid Mechanics: Mechanics of Turbulence.* Vol. 1, Dover Publications, 769 pp.

Peltier, W. R., and C. P. Caulfield, 2003: Mixing efficiency in stratified shear flows. *Annu. Rev. Fluid Mech.,* **35,** 135–167.

Pope, S. B., 2000: *Turbulent Flows.* Cambridge University Press, 802 pp.

Randall, D. A., 1980: Conditional instability of the first kind upside-down. *J. Atmos. Sci.,* **37,** 125–130.

Sherman, F. S., J. Imberger, and G. M. Corcos, 1978: Turbulence and mixing in stably stratified waters. *Annu. Rev. Fluid Mech.,* **10,** 267–288.

Siems, S. T., C. S. Bretherton, M. B. Baker, S. Shy, and R. E. Breidenthal, 1990: Buoyancy reversal and cloud-top entrainment instability. *Quart. J. Roy. Meteor. Soc.,* **116,** 705–739.

Smyth, W. D., and J. N. Moum, 2000: Length scales of turbulence in stably stratified mixing layers. *Phys. Fluids,* **12,** 1327–1342.

——, J. R. Carpenter, and G. A. Lawrence, 2007: Mixing in symmetric Holmboe waves. *J. Phys. Oceanogr.,* **37,** 1566–1583.

Stevens, B., 2002: Entrainment in stratocumulus-topped mixed layers. *Quart. J. Roy. Meteor. Soc.,* **128,** 2663–2690.

——, and Coauthors, 2003a: Dynamics and chemistry of marine stratocumulus—DYCOMS-II. *Bull. Amer. Meteor. Soc.,* **84,** 579–593.

——, and Coauthors, 2003b: On entrainment rates in nocturnal marine stratocumulus. *Quart. J. Roy. Meteor. Soc.,* **129,** 3469–3493.

Strang, E. J., and H. J. S. Fernando, 2001: Entrainment and mixing in stratified shear flows. *J. Fluid Mech.,* **428,** 349–386.

Tennekes, H., and J. L. Lumley, 1972: *A First Course in Turbulence.* MIT Press, 314 pp.

Thorpe, S. A., 1987: Transitional phenomena and the development of turbulence in stratified fluids: A review. *J. Geophys. Res.,* **92** (C5), 5231–5248.

Wang, S., J.-C. Golaz, and Q. Wang, 2008: Effect of intense wind shear across the inversion on stratocumulus. *Geophys. Res. Lett.,* **35,** L15814, doi:10.1029/2008GL033865.

Wood, R., 2012: Stratocumulus clouds. *Mon. Wea. Rev.,* **140,** 2373–2423.

Wunsch, S., 2003: Stochastic simulations of buoyancy reversal experiments. *Phys. Fluids,* **15,** 1442–1456.